Citation for final published version:

–

Boron-nitrogen-doped nanographenes: a synthetic tale from borazine precursors.

Jacopo Dosso, Tommaso Battisti, Benjamin D. Ward, Nicola Demitri, Colan E. Hughes, P. Andrew Williams, Kenneth D. M. Harris, and Davide Bonifazi*

[a] J. Dosso, T. Battisti, Dr. B. D. Ward, Dr. C. E. Hughes, Dr. P. A. Williams, Prof. Dr. K. D. M. Harris, Prof. Dr. D. Bonifazi; School of Chemistry, Cardiff University, Park Place, Cardiff CF10 3AT (UK). E-mail: bonifazid@cardiff.ac.uk.

[b] Dr. N. Demitri; Elettra - Sincrotrone Trieste, S.S. 14 Km 163.5 in Area Science Park, 34149 Basovizza - Trieste, Italy.

Keywords: polycyclic aromatic hydrocarbons, heteroatom doping, BN-doping, borazine, coronenes, gulf-type peripheries, optoelectronics, powder X-ray diffraction.

Abstract. In this paper we report a comprehensive account of our synthetic efforts to prepare borazino-doped hexabenzocoronenes using the Friedel-Crafts-type electrophilic aromatic substitution. We showed that hexafluoro-functionalized aryl-borazines, bearing an *ortho* fluoride leaving group on each *N-* and *B*-aryl rings, could lead to cascade-type electrophilic aromatic substitution events in the stepwise C-C bond formation giving higher yields of borazinocoronenes than those obtained with borazine precursors bearing fluoride leaving groups at the *ortho* positions of the B-aryl substituents. It is with this pathway that an unprecedented boroxadizine-doped PAH featuring a gulf-type periphery could be isolated, and its structure proved through single crystal X-ray diffraction analysis. Mechanistic studies on the stepwise Friedel-Crafts-type cyclisation suggest that the mechanism of the planarization reaction proceeds through extension of the π system. To appraise the doping effect of the boroxadizine unit on the optoelectronic properties of topology-equivalent molecular graphenes, the all-carbon and pyrylium PAH analogues, all featuring a gulf-type periphery, were also prepared. As already shown for the borazino-doped hexabenzocoronene, the replacement of the central benzene ring by its B_3N_2O congener widens the HOMO-LUMO gap and it dramatically enhances the fluorescence quantum yield.

Figure to table of contents
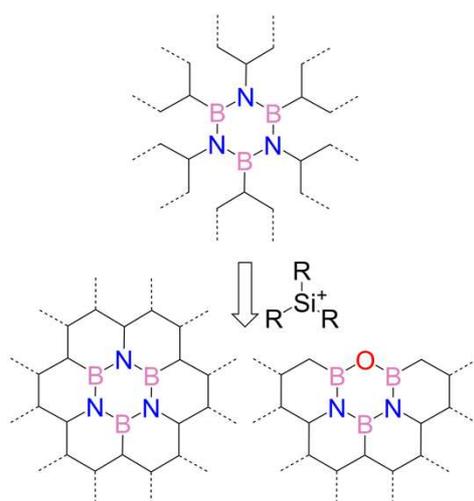
Introduction.

The doping of polycyclic aromatic hydrocarbons (PAHs) is currently emerging as one of the most promising approaches to tailor the optoelectronic properties of organic semiconductors.[1-4] The substitution of C=C bonds with isoelectronic and isostructural dipolar boron-nitrogen (BN)[5-7] and boron-oxygen (BO)[8-11] couples is an efficient method to gain control on the HOMO-LUMO band gap without significant structural modifications of the molecular scaffold.[12,13] The use of polar BN and BO bonds typically widen the HOMO-LUMO gap[14,15] and imparts dipole-driven self-assembly behaviors in the solid state[3,16] and on surfaces.[17-19] Noticeable examples include BN-doped pyrenes,[16] phenanthrenes,[20] anthracenes[21], perylenes[22,23] and nanographenes.[9,24-26] In these PAHs, the doping units are isolated BN couples selectively placed either at the peripheries or in the core of aromatic precursors bearing amino groups at specific positions. Another strategy consists in the use of preorganized doping units, in which the BN and BO couples are clustered in six-membered rings and used to replace benzenoid rings. Examples include the long-known inorganic $B_3N_nO_o$-based six-membered rings displayed in Figure 1: borazine (B_3N_3),[31] boroxadizine (B_3N_2O),[28-30] bordioxazine (B_3NO_2)[28,29] and boroxine (B_3O_3),[27].
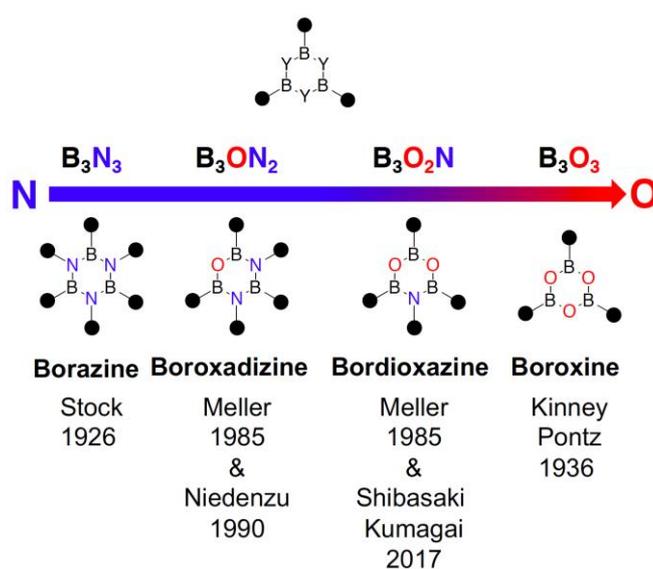

Figure 1. Inorganic $B_3N_nO_o$-based six-membered rings that can be used for doping graphenoid structures.

Amongst all inorganic rings, only the B_3N_3, B_3N_2O and B_3NO_2 units can be fully integrated into fully planarized nanographene systems. One can hardly fail to notice that the B_3N_3 ring can replace any benzenoic units in a molecular graphene scaffold, whereas the B_3N_2O and B_3NO_2 rings can only be placed at the peripheries. For instance, a bordioxazine-fused PAH displaying catalytic activity in the dehydrative amidation of carboxylic acids and amines has been very recently reported by Shibasaki and Kumagai.[32] Borazine derivatives have been mainly used as precursors to build BN-doped graphitic-like carbon materials. Important examples include graphenes[33-35] and polymers.[36-40] On the other hand, the use of the boroxadizine ring to dope PAHs remains elusive to the best of our knowledge.

Certainly, the most intriguing example in the field is that of hexabenzoborazinocoronene (**1**), the B_3N_3-doped congener of hexabenzocoronene (**HBC**), that can be considered as the smallest borazino-doped nanographene structure (Scheme 1). Bettinger and co-workers firstly reported the thermolytic synthesis of **1**, in which the central benzene ring has been replaced by a borazine core (Scheme 1).[34] In a parallel avenue, our group contributed to the field with the engineering of borazine-doped polyphenylenes[37,40] and reported the rational synthesis of a soluble derivative of **1**, molecule **2**,[33] through six intramolecular Friedel-Crafts-type reactions[33,41] using a hexafluoro-functionalized borazine precursor (Schemes 1-2). In our synthetic approach the fluoride leaving groups are placed at the *ortho* positions of the B-aryl substituents in the borazine precursors and the electrophilic aromatic substitution reaction led to molecule **2** in 5% yield along with a non-cyclic helicoidal side-product **7** (Scheme 2). Capitalizing on the Friedel-Crafts-type electrophilic aromatic substitution,[41] herein we report a comprehensive account of our synthetic efforts to prepare borazino-doped hexabenzocoronenes. Aiming at enhancing the yield of soluble borazinocoronene **2**, we reasoned that the hexafluoro-functionalized isomer of molecule **5**, bearing an *ortho* fluoride leaving group on each *N*- and *B*-aryl rings, could lead to cascade-type electrophilic aromatic substitution events in the stepwise C-C bond formation. It is during these synthetic investigations that we could isolate the first boroxadizine-doped PAH featuring a gulf-type periphery and prove its structure through single

crystal X-ray diffraction analysis. Propelled by these findings, we decided to investigate further the doping effect of the boroxadizine unit and prepared all-carbon and pyrylium[42-45] PAH analogues, all featuring a gulf-type[46] periphery. As observed for the case of molecule **2**, the replacement of the central benzene ring by its B_3N_2O congener widens the HOMO-LUMO gap and it enhances the fluorescence quantum yield. Xylyl moieties were introduced to favor solubility.
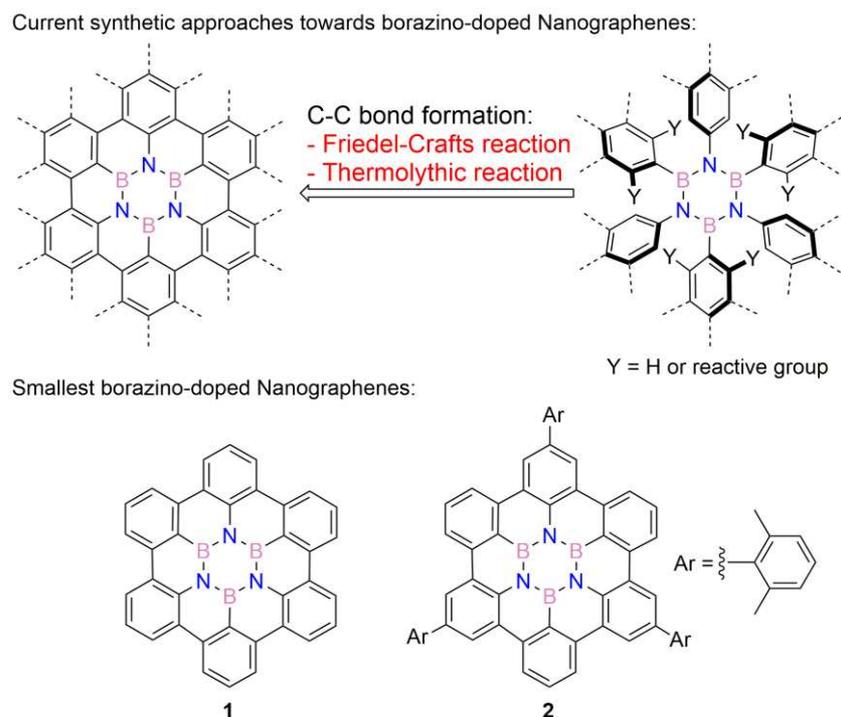
Scheme 1. Synthetic planarization protocols for preparing borazino-doped hexabenzocoronenes **1** and **2**.

Results and discussion.

Synthesis and structure determination of BN-doped nanographenes. In our early report,[33] we prepared B_3N_3-doped hexabenzocoronene **2** capitalizing on the Friedel-Crafts reaction using difluoroarenes (route A, Scheme 2).[41] In this strategy, hexafluoro borazine **5** was obtained after reaction of 4-xylyl aniline **3** with BCl_3 followed by addition of 2,6 difluorophenyl lithium **4** (Scheme 2).[33] Subsequent planarization with $[iPr_3Si-CB_{11}H_6Cl_6]$ and Me_2SiMes_2 at 110 °C in PhCl, gave molecule **2** (5% yield) and partially fused BN-derivative **7** as the major product (17% yield). Further purification of the reaction mixture allowed us to isolate partially fused derivative **A1**. Also, mass analysis investigations showed that molecular ions corresponding

to **A2** were present in the reaction crude (see below for the hypothesized stepwise cyclization mechanism).
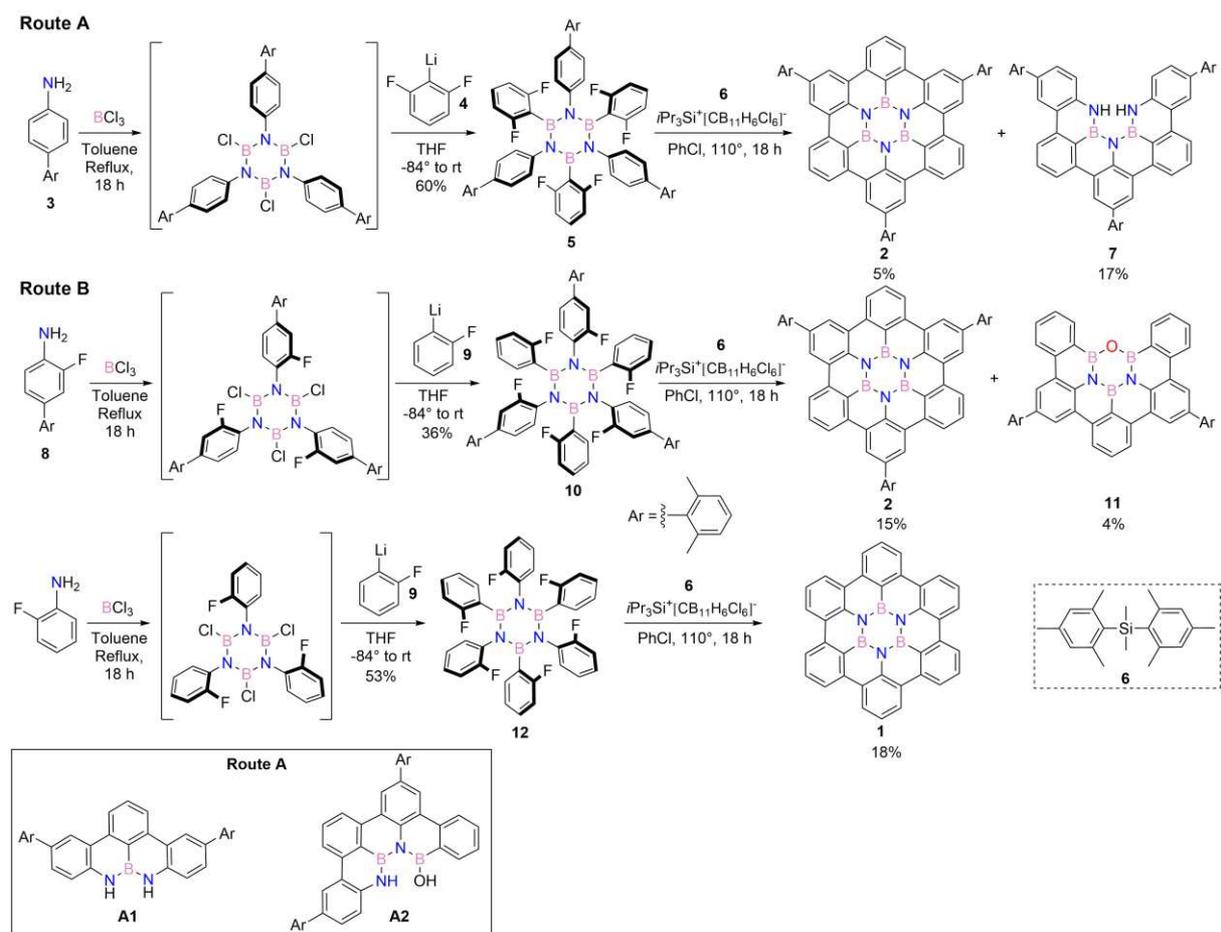
Scheme 2. Routes A and B for preparing BN-doped nanographenes.
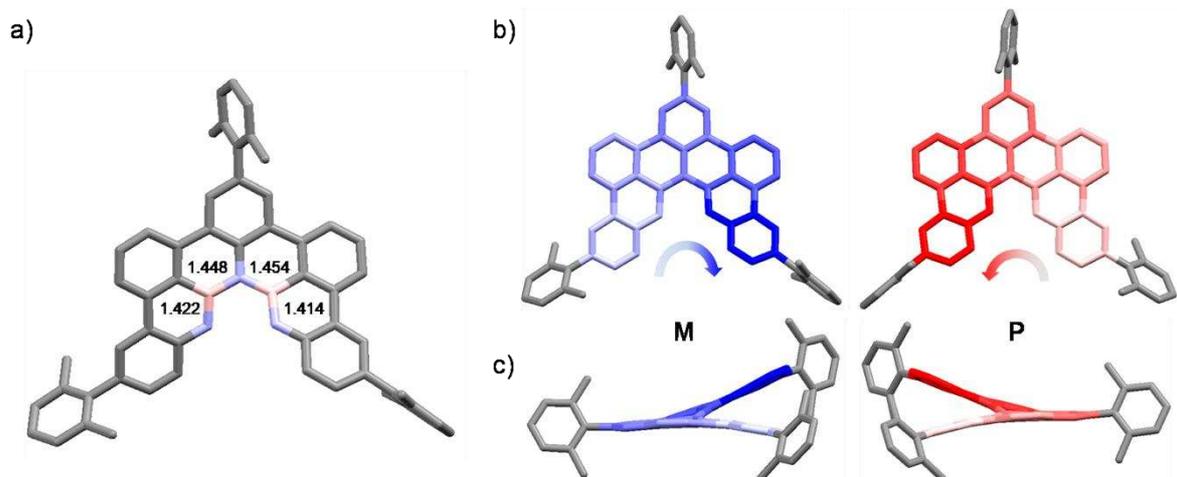
Figure 2. a) Front view of **7** with BN distances b), c) front view and side view with axial enantiomers (M and P highlighted) of **7**. Atom colors: pink B, blue N, gray C; space group: $P\,2_1/n$.

The structure of derivative **7** was further confirmed by single-crystal X-ray analysis (Figure. 2), which displayed an helicene-like arrangement, with a 37° tilt around a central cove periphery. The BN bond lengths for **7** are: 1.414(4)-1.422(3) Å for the BNH couple and 1.448(3)-1.454(4) Å for the NBN fragment, slightly different from those reported for **2** (1.433(3)-1.442(2) Å).

Aiming at improving the reaction yield, we redesigned the borazine precursor and prepared a BN-derivative bearing one fluorine atom on the *ortho*-position of each ring (route B, scheme 2). In this synthetic route, aniline **8** is reacted with BCl_3 in refluxing toluene, followed by the addition of 2-fluorophenyl lithium **9** to give hexafluoro borazine derivative **10** in a 36% yield. Subsequent ring-closure reaction in the presence of Me_2SiMes_2 and $[iPr_3Si-CB_{11}Cl_6H_6]$ at 110°C in degassed PhCl afforded borazino-coronene **2** in 15% yield. While purifying the reaction mixture, an additional product was isolated in a 4% yield. To our surprise the product proved to be B_3N_2O-doped PAH **11** featuring a gulf-type periphery. To the best of our knowledge, this molecule is the first example of a PAH embedding a B_3N_2O cycle. To validate its chemical structure, crystals suitable for X-ray diffraction were grown, and the resulting structure is displayed in Figure 3. Focusing on the bond lengths in the B_3N_2O ring, the BN distances varies between 1.437(4) Å and 1.441(4) Å, similarly to the values reported for molecule **2**.[33] The BO bond lengths are 1.386(4) and 1.375(4), very close to the distances measured for boric acid and phenyl boroxine.[47]
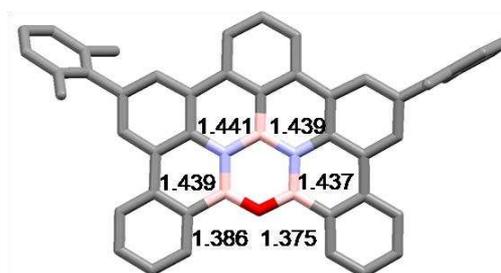
Figure 3. Front view of molecule **11** with BN and BO bond lengths. Atom colors: pink B, blue N, red O, gray C; Space group: *P* $2_1/c$.

To probe the versatility of route B, we undertook the synthesis of unsubstituted borazinocoronene **1**, and prepared hexafluoro borazine **12**. As for intermediate **10**, each B- and N-aryl rings in precursor **12** bear an *ortho*-fluoride atom (Scheme 2). Friedel-Crafts reaction led to **1**

as an insoluble material, whose structure was confirmed by mass-spectrometry in line with the seminal report by Bettinger and co-workers.[34] Given the insolubility of molecule **1**, we have carried out structure determination from powder X-ray diffraction data.

Crystal structure determination of molecule 1 from powder XRD data. A previous powder XRD study has been reported[34] for **1**, involving profile-fitting (using the Le Bail technique) of the powder XRD pattern recorded for a two-phase sample comprising **1** together with another crystalline phase arising from one of the reagents involved in the synthesis. The Le Bail fitting showed that the unit cell of **1** closely matches the unit cell in the reported crystal structure[48,49] of hexa-*peri*-hexabenzocoronene (which contains a central C_6 ring instead of a B_3N_3 ring). However, the previous powder XRD study[34] only considered the preliminary profile-fitting stage of the structure determination process, and did not proceed to carry out structure solution and refinement. The powder XRD pattern of **1** prepared in the present work closely matches that reported previously,[34] but in our case it is clear from the powder XRD pattern that our sample is a pure phase of **1** (see below). This powder XRD pattern was used for structure determination of **1**.

Fitting and unit cell refinement from the powder XRD data were carried out using the Le Bail technique[50] implemented in the program GSAS,[51] starting from a unit cell (a = 12.929 Å, b = 5.119 Å, c = 17.9983 Å, β = 108.984°) and space group (P2$_1$/n) that were derived from the reported[49] unit cell of the carbon analogue of **1** by transformation to the conventional setting (which has the shortest lengths of the a- and c-axes and the value of β closest to 90°). A good-quality Le Bail fit was achieved (Figure 4a; R_{wp} = 0.57%, R_p = 0.44%), with the following refined unit cell parameters: a = 12.921(5) Å, b = 5.0996(7) Å, c = 18.002(5) Å, β = 109.151(16)°. The fact that this unit cell accounts for all peaks observed in the experimental powder XRD data confirms the assignment of the sample as a pure crystalline phase. From the unit cell volume and density considerations, it is deduced that are two molecules of **1** are in the unit cell, and therefore the asymmetric unit for space group P2$_1$/n comprises one half molecule of **1**.

Structure solution of **1** was carried out using the direct-space strategy,[52,53] implemented using a genetic algorithm (GA) in the program EAGER.[54-61] In the direct-space structure solution calculations (see SIfor more details), the molecular model was derived from the molecule in the crystal structure[49] of the carbon analogue of **1**, but with the central C_6 ring replaced by a central B_3N_3 ring. The asymmetric unit comprised the whole molecule of **1** with half occupancy of all atoms, and with the centre of the molecule fixed at a crystallographic inversion centre. Clearly, the inversion symmetry operation creates disorder in the positions of the B and N atoms in the central ring, resulting in an occupancy of $B_{0.5}N_{0.5}$ for each atomic site in the central ring. The trial structure giving the best fit to the experimental powder XRD data (i.e., lowest R_{wp}) in the structure solution calculations was used as the initial structural model for Rietveld refinement (see SI for more details), which was carried out using the program GSAS.[51] The final Rietveld refinement produced a good-quality fit (Figure 4b; R_{wp} = 0.60%, R_p = 0.45%), comparable to the quality of fit obtained in the Le Bail fitting procedure (Figure 4a), with the following refined unit cell parameters: a = 12.934(5) Å, b = 5.1022(8) Å, c = 18.009(5) Å, β = 109.188(17)°, V = 1122.4(7) $Å^3$.
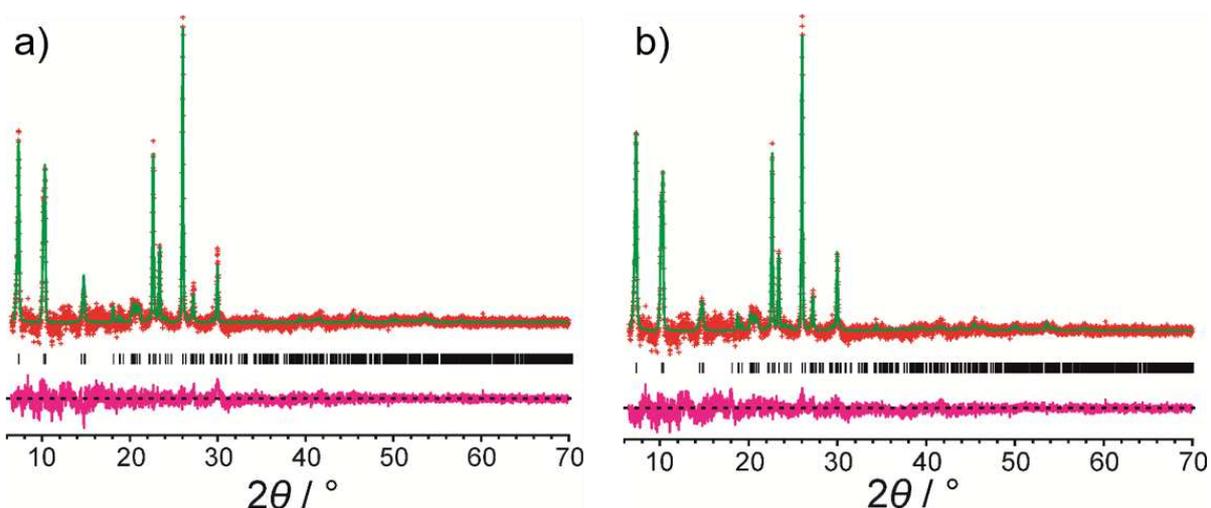
**Figure 4.** a) Le Bail fitting of the powder XRD pattern of **1**, and b) final Rietveld refinement for **1**. Red + marks, experimental data (background subtracted); green line, calculated data; magenta line, difference plot; black tick marks, predicted peak positions.

The crystal structure of **1** (Figure 5a,b), is essentially iso-structural to the crystal structure of the carbon analogue,[49] as

demonstrated by the overlay of the two structures in Figure 5c. According to the classification of aromatic hydrocarbon crystal structures,[62] the structure is assigned to the γ packing type. The molecules are arranged in "slabs" parallel to the *ab*-plane; all molecules in a given slab are related by translation and hence have the same orientation. Adjacent slabs are related by the 2_1 screw axis (parallel to the *b*-axis), and the molecules in adjacent slabs have different orientations. As discussed above, the crystal structure of **1** is disordered, with each atomic site in the central ring represented as $B_{0.5}N_{0.5}$. This representation of the average structure may be readily interpreted in terms of the molecule of **1** adopting two orientations with equal probability (the two orientations differ by 60° rotation about an axis perpendicular to the plane of the molecule). In the average structure, the positions of the C and H atoms for the two orientations occupy the same set of sites.
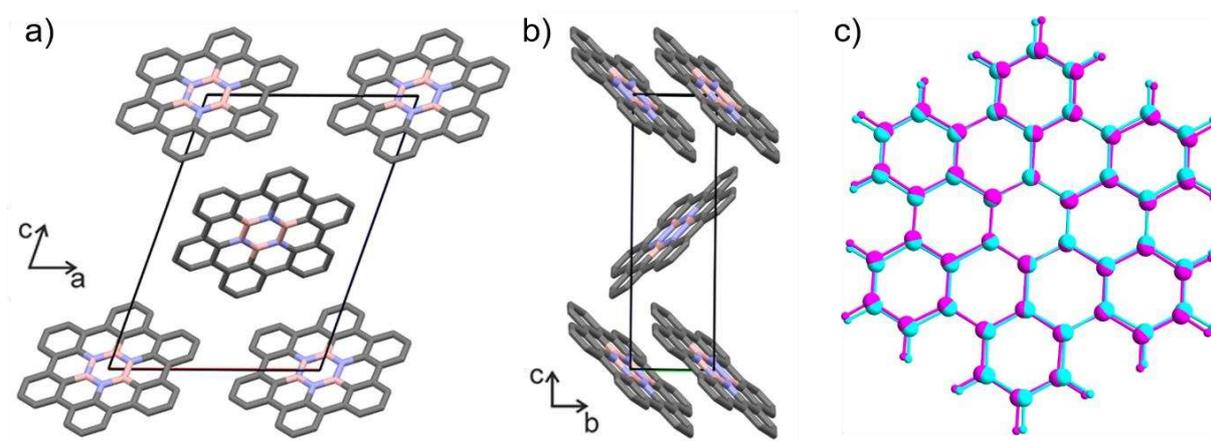
Figure 5. Crystal structure of **1** viewed a) along the *b*-axis and b) along the *a*-axis. In this disordered structure, the occupancy of each atomic site in the central ring is $B_{0.5}N_{0.5}$. The slabs of molecules discussed in the text are parallel to the *ab*-plane, which is horizontal in both (a) and (b). c) Overlay of the crystal structures of **1** (magenta) and the carbon analogue of **1** (cyan). The overlay was constructed by matching the unit cell axes (not shown) of the two structures.

To assess whether there is any significant energy difference between the two molecular orientations in the disordered (average) structure, periodic DFT-D calculations were carried out for two ordered structures, in each case containing only one of the two molecular orientations. To generate these ordered structures, the crystallographic inversion centre was removed to give space group $P2_1$ (with one molecule in the asymmetric unit), and the central ring was

an ordered B_3N_3 ring (i.e., with each atomic site occupied by only B or only N, and with the B and N atoms alternating around the ring). The two ordered structures differ by 60° rotation about an axis perpendicular to the plane of the molecule. Each structure was subjected to DFT-D geometry optimization (with fixed unit cell). The resulting geometry optimized structures are very similar (except in regard to the assignment of B and N atoms to the atomic sites of the central ring); the largest displacement between atomic sites in the two structures is 0.111 Å, with an RMSD of 0.072 Å. The energy difference between the two optimized structures is only 4×10^{-4} kJ mol^{-1}. This very small energy difference is fully compatible with the existence of disorder involving equal populations of the two molecular orientations in the average crystal structure determined from powder XRD data.

Computational investigations of the stepwise Friedel-Crafts planarization reaction. To rationalize the synthetic outcomes of the Friedel-Crafts reaction and set future bases to improve the reaction protocols for preparing borazine-doped nanographenes, we decided to study the mechanistic details of the planarization reaction. When looking at the structures of side-products **7** and **11**, one hardly fails to see that these compounds can only derive from partially cyclized intermediates, in which a substituent is cleaved possibly following a hydrolysis. Similarly, the presence of side-products **A1** and **A2** suggests that hydrolysable intermediates with a lower degree of annulation are also formed in the reaction mixture. Taken all together, these observations prompted us to hypothesize that the ring-closing Friedel-Crafts reactions occur stepwise (i.e., through six cyclization reactions, labelled here as c_1-c_6). Considering that the transition state for each endothermic cyclization resembles the intermediate more than the precursor,[63] we studied the planarization reactions through computational simulations of the intermediates that are possibly formed in each annulation step. The structures of all postulated intermediates in the Friedel-Crafts reactions were calculated using density functional theory calculations (with B3LYP hybrid functional,[64] with a 6-31(d,p) basis set[65] on all centres) with Gaussian 09.[66] Solvent THF was incorporated using the polarized continuum model, in which the molecular cavity is defined by the united

atom model that incorporates hydrogen into the parent heavy atom.[67] The relative energies ($\Delta\Delta$G) are provided in Schemes 3 and 4 and are reported relative to the lowest energy isomer in each cyclization subset. To ease the nomenclature of the intermediates, the structures are labelled as $\mathbf{5}^{\boldsymbol{n}}_{\boldsymbol{ci}}$ and $\mathbf{10}^{\boldsymbol{n}}_{\boldsymbol{ci}}$ for synthetic routes A and B, respectively, with n standing for the intermediate within the cyclization subset, and ci the cyclization step. For pathway A, it is clear that only an intermediate can be envisaged for cyclization reactions $c1$ and two for $c5$, whereas up to four isomers could be formed within cyclization subsets $c2$-$c4$ (Scheme 3). Since we used an isomeric mixture of the starting hexafluoro borazine for pathway B, one can envisage a complicated pattern of intermediates, including two for cyclization subsets $c1$ and $c5$, eight for $c2$, fourteen for $c3$, and seven for $c4$ (Scheme 4). The fact that the formation of the B_3N_2O-doped product should derive from the hydrolysis of an intermediate formed within the cyclization subset $c4$, led us to restrict our calculations to the intermediates formed in steps $c4$ and $c5$. When looking at the relative energies of the intermediates, it is evident that the lowest energy intermediate for each cyclization subset ($\mathbf{5}^{\boldsymbol{a}}_{\boldsymbol{c2}}$, $\mathbf{5}^{\boldsymbol{a}}_{\boldsymbol{c3}}$ and $\mathbf{5}^{\boldsymbol{a}}_{\boldsymbol{c4}}$ for pathway A; $\mathbf{10}^{\boldsymbol{a}}_{\boldsymbol{c4}}$ and $\mathbf{10}^{\boldsymbol{a}}_{\boldsymbol{ci}}$ for pathway B) is that displaying the greatest degree of planarity in the central B_3N_3 ring. A convenient method to quantify the planarity of the B_3N_3 ring is to calculate the RMS deviation of the B atoms from a plane defined by the three N atoms. RMSD analysis show that the smallest values (0.083, 0.242 and 0.130) are observed for the lowest energy intermediates $\mathbf{5}^{\boldsymbol{a}}_{\boldsymbol{c2}}$, $\mathbf{5}^{\boldsymbol{a}}_{\boldsymbol{c3}}$, and $\mathbf{5}^{\boldsymbol{a}}_{\boldsymbol{c4}}$ (Table S2). Interestingly, when looking at the isolated side-products in route A (Scheme 3), it is clear that products **A1**, **A2**, and **7** derive from the hydrolysis of intermediates $\mathbf{5}^{\boldsymbol{a}}_{\boldsymbol{c2}}$, $\mathbf{5}^{\boldsymbol{a}}_{\boldsymbol{c3}}$, and $\mathbf{5}^{\boldsymbol{a}}_{\boldsymbol{c4}}$, respectively, which lie on the lowest energy pathway. These observations suggest the occurrence of a planarity-driven cyclization mechanism. After the first electrophilic substitution leading to a flat phenanthrene-like substructure ($\mathbf{5}_{\boldsymbol{c1}}$), the second favored reaction occurs at one of the phenanthrene periphery, further extending the conjugation of the π-surface ($\mathbf{5}^{\boldsymbol{a}}_{\boldsymbol{c2}}$). The subsequent cyclization reactions ($c3$-$c5$) occur stepwise progressively extending the outer π-conjugated rim until the last annulation $c6$ lead to final hexabenzoborazinocoronene derivative (Scheme 3).
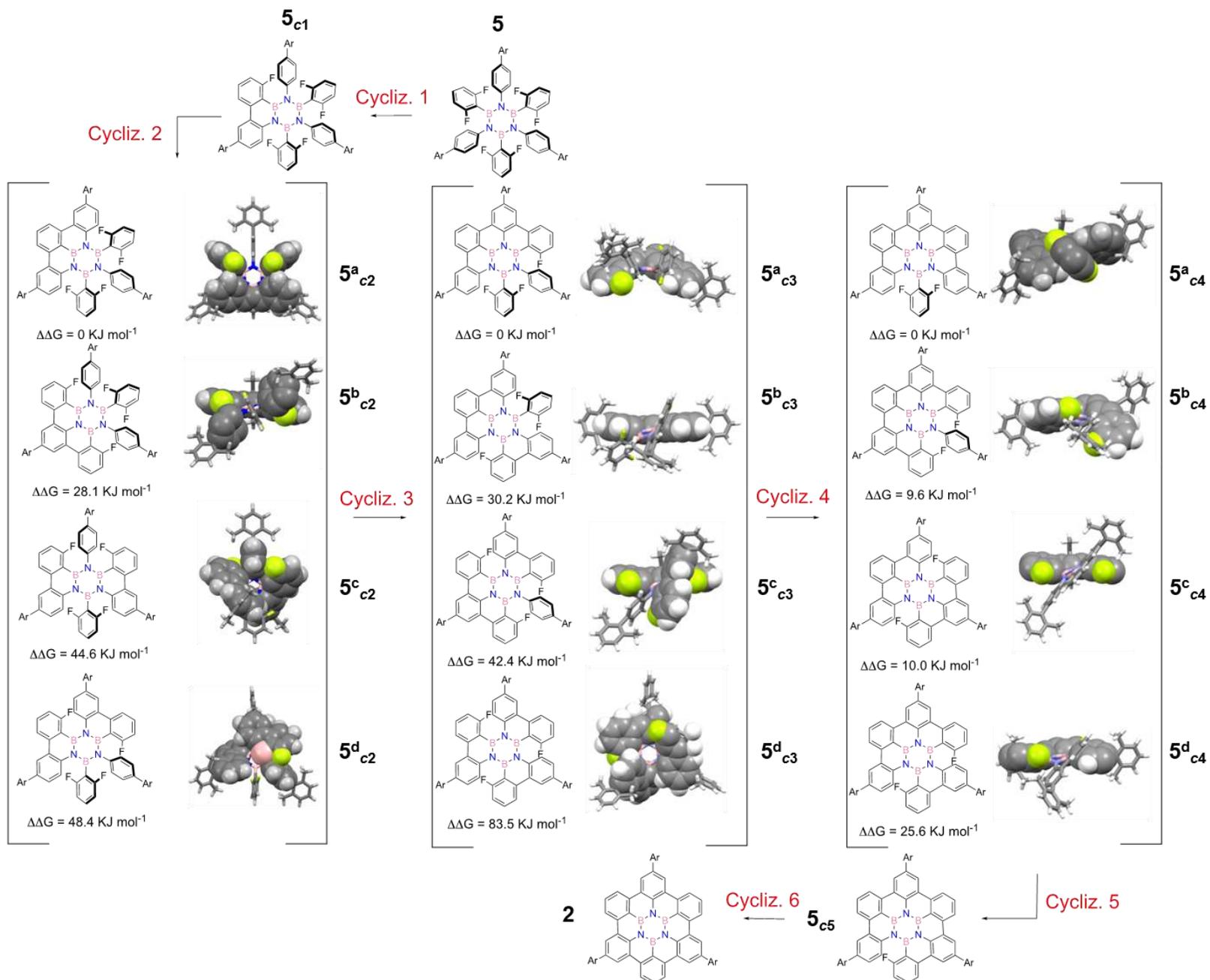
Scheme 3. Step wise Friedel-Crafts-based planarization mechanism according to route A. Calculated Gibbs free energies (ΔΔG) for the possible intermediates formed at each cyclization step [B3LYP/6-31G(d,p)].
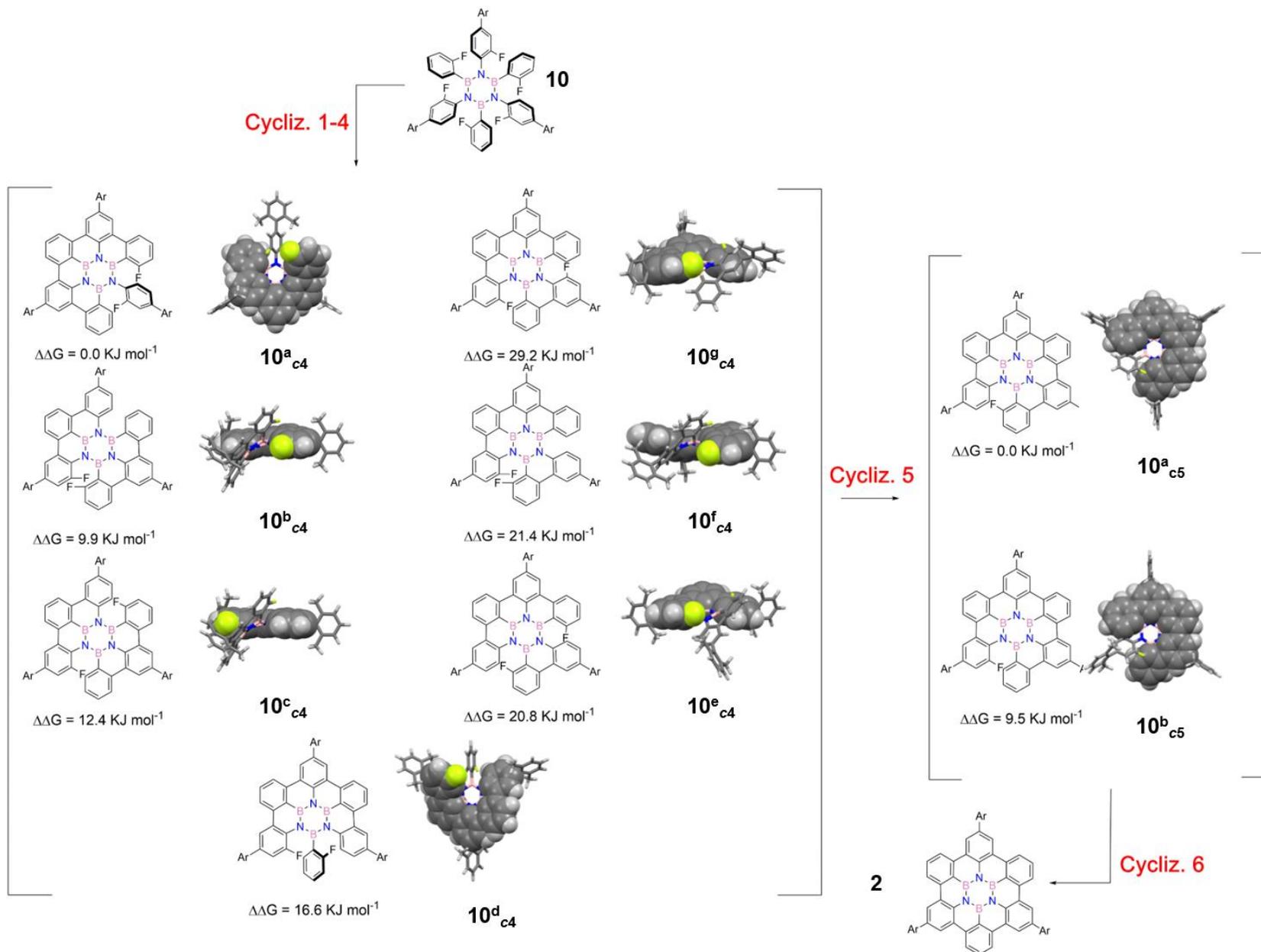
Scheme 4. Friedel-Crafts-based stepwise planarization mechanism according to route B. In this case, the calculated Gibbs free energies (ΔΔG) of the intermediates intervening in the fourth and fifth cyclization steps are considered. The presence of different isomers in steps 1-3 deterred us from tackling the calculation of all steps [B3LYP/6-31G(d,p)].

A similar planarity-driven cyclization mechanism to that proposed for route A, can be envisaged for route B (Scheme 4), in which the lowest energy intermediates for $c4$ and $c5$ are intermediates $\mathbf{10^a_{c4}}$ and $\mathbf{10^a_{c5}}$. One can hardly fail to notice that the B_3N_2O-doped derivative **11** possibly derives from the hydrolysis of intermediate $\mathbf{10^a_{c4}}$ after replacement of a fluorine with a hydrogen atom. At the present time, further investigations are needed to unravel the possible source of hydride yielding the fluoride-hydrogen exchange reaction. Complementary mass-spectrometric analysis of the reaction mixtures depicted the presence of the molecular ion associated to one of the intermediates from $c5$, further supporting our theoretical investigations and mechanistic hypothesis.

The greater stability of a planar borazine ring is somewhat intuitive, when considering that a planar system has a greater degree of delocalization in the π-system. However, this electronic explanation can be given increased rigor using Natural Bonding Orbital (NBO) analyses of the calculated structures. NBO analysis of the parent borazine **5** indicates two 3-centre, 4-electron hyperbonds in the B_3N_3 core, each centered about a NBN unit and described as a combination of a N-centered p orbital and a BN π bond as NB:N↔N:BN (Figure 6, left), thus describing a strongly delocalized structure. The NBO analyses of those species that deviate from planarity indicate substantially less-delocalized structures. Using $\mathbf{5^c_{c2}}$ as a representative example in which the boron atoms deviate most from planarity within the series, the NBO analysis does not find the 3-centre 4-electron hyperbond (a significant indicator of extensive delocalization), but second-order perturbation analysis indicates a number of donor-acceptor interactions that involve the N-based occupied p orbitals and the B-based vacant p orbitals, thereby indicating a lesser degree of delocalization (Figure 6, right). In intermediate $\mathbf{5^c_{c2}}$ one of the boron atoms lies on the plane defined by the three N atoms (B_{plane}, deviation from plane = 0.001 Å), whereas the other two lie above and below the plane in equal and opposite directions ($B_{out-of-plane}$,

deviation from plane = 0.441 Å); the NB$_{plane}$ p–p interactions are calculated to have a greater strength (84 kcal) than the equivalent NB$_{out-of-plane}$ interactions (73 and 28 kcal), thus giving a rational explanation for the calculated stabilities of the two intermediates.
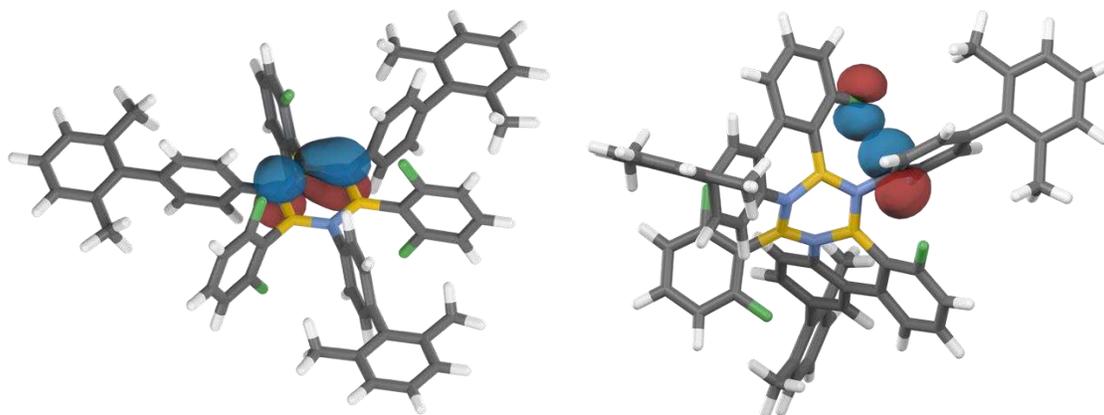

Figure 6. Left: A 3-centre, 4-electron bond described by NBO analysis of precursor **5**; right: NBO-derived donor-acceptor interaction between a fluorine lone pair and an ipso carbon of the aryl group in **5$^{c}_{c2}$** [B3LYP/6-31G(d,p)].

At last, it is noteworthy that the mean deviation of the borazine ring from planarity does not directly correlate with their relative free energies; for example, **5$^{c}_{c2}$** has the greatest deviation from planarity (RMSD = 0.294 Å; $\Delta\Delta G$ = 44.6 kJ mol^{-1}) from the **5$^{a}_{c2}$**–**5$^{d}_{c2}$** series but **5$^{d}_{c2}$** has the highest relative free energy (RMSD = 0.250 Å; $\Delta\Delta G$ = 48.4 kJ mol^{-1}). The relative free energy of **5$^{c}_{c2}$** is lower than expected owing to an extraneous stabilizing effect relating to the unlinked non-fluorinated aryl group *via* two donor-acceptor interactions from the proximal fluorine lone pairs to a lone valence (vacant *p* orbital) on the ipso-carbon of the aryl moiety (Figure 6). These analyses give an overall picture of the BN delocalization being the dominant factor in determining stability, but where comparatively minor stereoelectronic factors can have a significant contribution to the overall stability of intermediate species in the reaction process.

Synthesis of pyrylium and all-carbon gulf-type congeners of the B₃N₂O-doped PAH. Following the unexpected isolation of B$_3$N$_2$O-doped PAH **11,** we decided to prepare its all-carbon (**18**) and pyrylium (**26**) gulf-type analogues and evaluate the effect of doping of the central benzenoid ring. Our syntheses started with the preparation of **18** (Scheme 5). The synthetic path started with a trimerization reaction of a 1:2 mixture of acetophenone and 2'-bromoacetophenone in the presence of a catalytic amount of TfOH at 130 °C. The reaction produced an inseparable mixture of bromo-terphenyl derivatives (**13**), that was directly used in a Suzuki cross coupling with **14.** Subsequently, the isomeric mixture was demethylated using BBr$_3$ in CH$_2$Cl$_2$, yielding a combination of hydroxyl derivatives that could be separated using silica gel column chromatography to give targeted molecule **15** in 23% yield (over 2 steps).
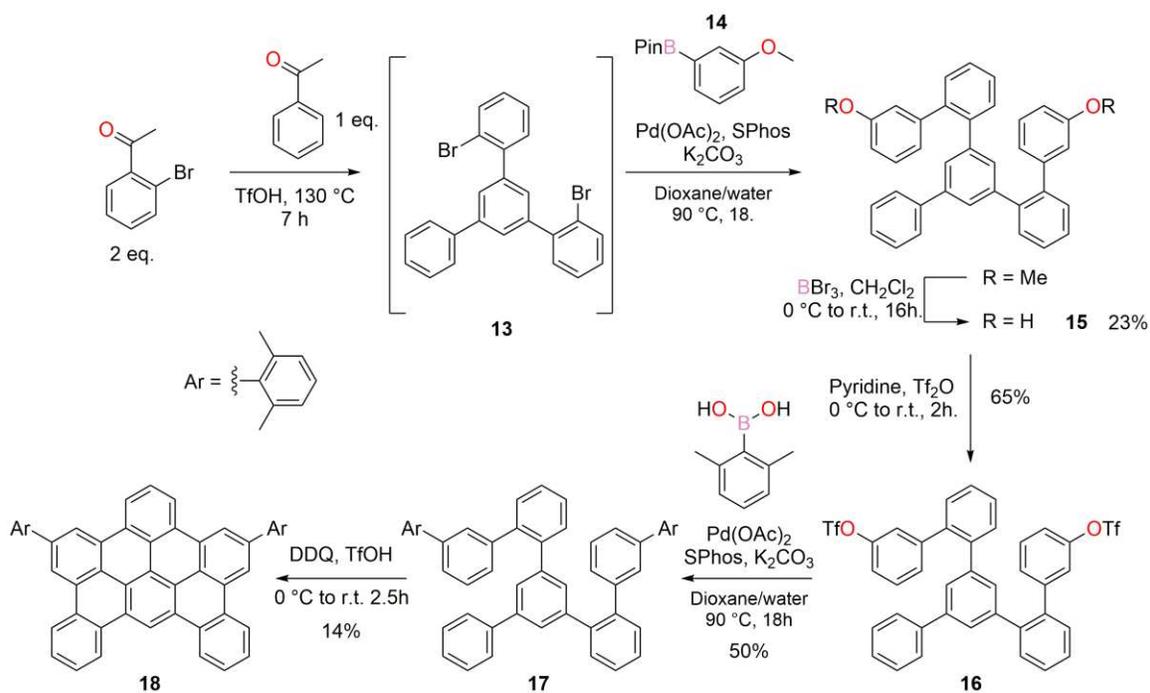
Scheme 5. Synthetic pathway for preparing full-carbon gulf congener **18.**

Reaction of **15** with (Tf)$_2$O in pyridine afforded triflate **16,** which was cross-coupled with (2,6-dimethylphenyl)-boronic acid under typical Suzuki conditions to give final polyphenylene derivative **17.** Finally, oxidative ring closure reaction was achieved using

DDQ and TfOH to give planarized derivative **18** with a 14% yield. Next, we proceeded with the preparation of the pyrylium gulf-type analogue, molecule **26** (Scheme 6).[45] Suzuki cross-coupling reaction between (2,6-dimethylphenyl)-boronic acid and 4-iodo-2-bromo-toluene gave bromo-aryl derivative **19** in the presence of $Ba(OH)_2$ as base.[68] Molecule **19** was then converted to boronic ester **20** (63%) under Miyaura borylation reaction conditions. Successive Pd-catalyzed cross-coupling reaction led to the formation of amide **22** in a 73% yield (Scheme 6). Cyclization reaction triggered by an amide-directed *ortho*-lithiation and subsequent addition-elimination reaction on the amide group, gave phenanthrol **23** in almost quantitative yield.
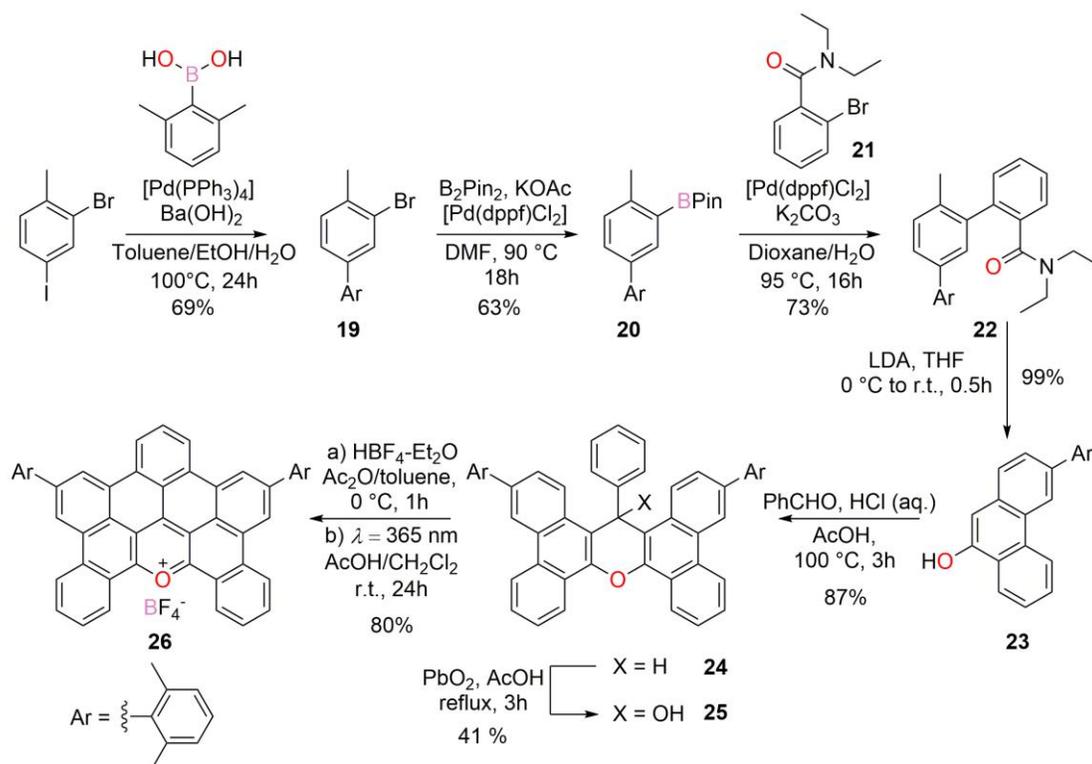
Scheme 6. Synthetic pathways for preparing gulf pyrylium congener **26**.

Aldolic condensation between phenanthrol **23** and benzaldehyde in the presence of HCl yielded xanthene derivative **24** that, by treatment with PbO_2, gave desired xanthenol **25** with a 41% yield (Scheme 6). At last, xanthenol **25** was treated with $HBF_4 \cdot Et_2O$ and

the resulting orange precipitate irradiated at 365 nm in a CH_2Cl_2/AcOH solution to give desired pyrylium **26** in high yield (80%). The structures of all intermediates and targeted compounds were characterized by spectroscopic and spectrometric techniques. Suitable crystals for X-ray diffraction analysis for the all-carbon structure **18** were obtained (Figure 7d).
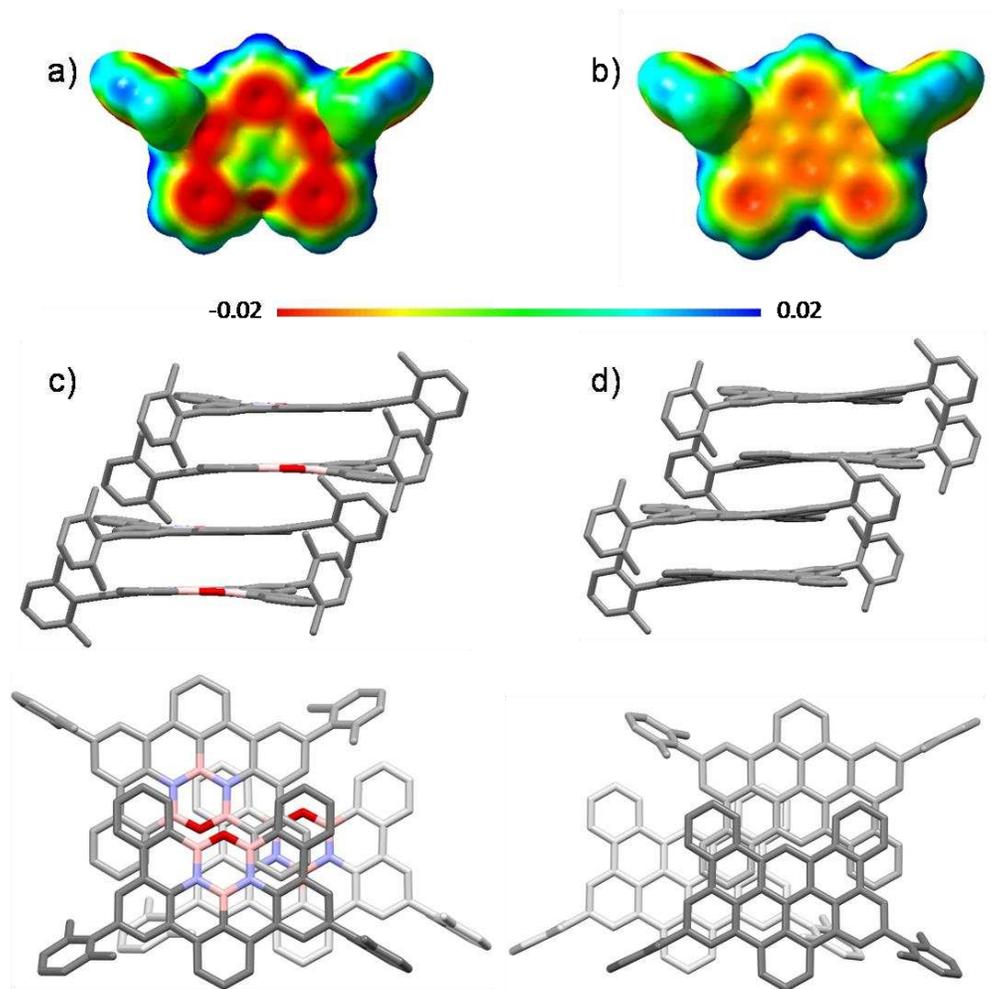
Figure 7. ESP surfaces mapped on the vdW surface up to an electron density of 0.05 electron/bohr^{-3} for a) **11** and b) **18**. Side (up) and top (bottom) view of the packing of c) **11** and d) **18**. Atom colors: pink B, blue N, red O, gray C. Space groups: *P* $2_1/c$ and *P*–1.

No crystals for pyrylium **26** could be formed despite numerous attempts. To better understand the differences in the charge distribution between **11** and **18**, ESP surfaces were plotted (Figure 7a-7b). Molecule **18** shows an extended π-surface with low

electrostatic potential, instead the presence of the inorganic ring in congener **11** induces a relatively high potential region with a strong polarization, with positively charged B atoms and negatively charged N and O atoms (Figures 7a-b). Interestingly, the aromatic sextets in **11** depict considerably negative electrostatic potentials compared to those in **18**. The X-ray crystal structures of **11** (Figure 7c) and **18** (Figure 7d) provide further confirmation of the flat nature of both PAHs (average RMSD of the atoms in the aromatic scaffold from their mean plane is 0.13(9) Å for **11** and 0.15(12) Å for **18**). The molecules undergo $\pi\cdots\pi$ stacking interactions, with the molecular units arranged antiparallelly into columns with average distances of 3.52(20) Å and 3.43(16) Å for **18** and **11**, respectively.

NMR properties of the heteroatom-doped nanographenes. To study the effect of doping units on the ring current properties, we compared the ^{1}H-NMR spectra of PAHs **11**, **18** and **26** (Figure 8b$_1$-b$_3$). As the diagnostic proton resonance, we selected the chemical shift (δ_{Ha}) of the H_a proton, which is 8.82 ppm for **11**, 9.30 ppm and 9.77 ppm for **18** and **26**, respectively. To shed further light on the effects of different doping units on the magnetic properties, GIAO-NICS(1) calculations were also performed (Figure 8a). The replacement of the central benzenoid ring with the B_3N_2O cluster causes a strong change in the NICS value from -12 ppm (aromatic) to -0.95 ppm (non-aromatic) in the central region of the molecule. A similar change in the NICS value has been also observed for the non-sextet rings of the Clar resonance structure surrounding the B_3N_2O system, where a shift from an average of -2.68 in **18** to -0.79 ppm in **11** was observed.[69] This effect seems to confirm the enhancement of the localization of the aromatic sextets induced by the presence of the central B_3N_2O ring.[12] Molecule **26** depicts intermediate magnetic properties between those observed for **11** and **18**, with a -6.5 ppm shift for the central ring (Figure 8a, molecule **26**), whereas the other all-carbon rings feature an overall magnetic anisotropy similar to that calculated for **18** (Figure 8a). ACID calculations

were also performed for the derivatives (Figure S74), revealing to be in full agreement with the NICS(1) predictions.
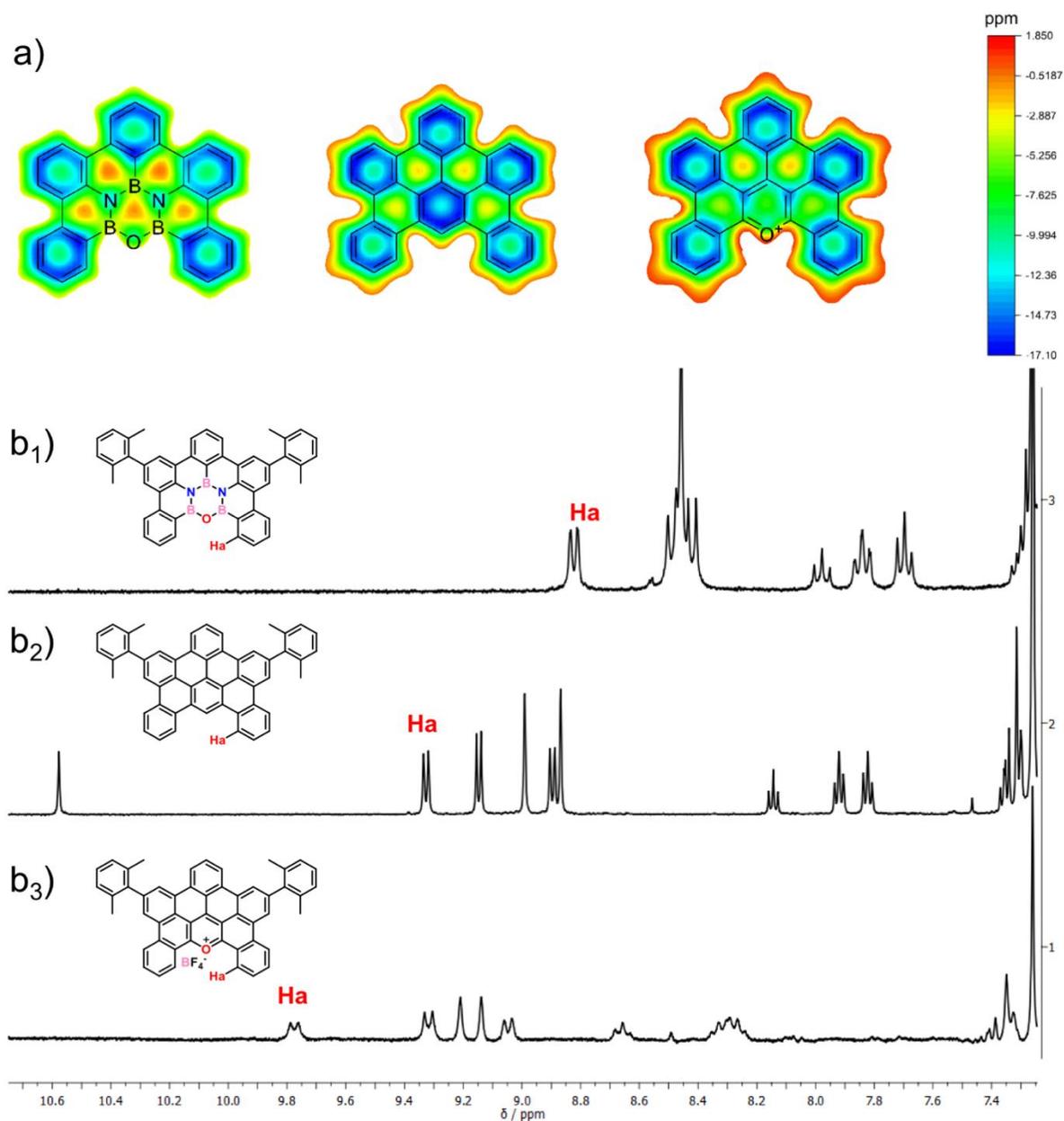
Figure 8. a) NICS(1)-GIAO surfaces for **11**, **18**, and **26** calculated from the B3LYP/6-31+G** optimized geometry in vacuum; b) Exerts of the ^{1}H-NMR spectra (400 MHz, CDCl$_3$) in the aromatic region for **11** (above), **18** (center), and **26** (below).

The experimental data for the δ_{Ha} of molecules **11** and **18** are fully consistent with both ACID and NICS calculations, on the other hand, further discussion is required for the δ_{Ha} value observed for the

pyrylium congener. If one solely considers the NICS calculations, the δ_{Ha} value for molecule **26** should fall in 8.87-9.30 ppm range. However, the electron deficient character of the carbon atom attached to H_a proton further deshields the latter, leading to the highest experimental δ_{Ha} value in the series. As previously observed for molecules **2** and **HBC**,[33] these data strengthen our hypothesis for which the replacement of an all-carbon fully benzenoid six-membered ring with an inorganic congener, *e.g.* B_3N_2O and B_3N_3, reduces the aromatic character of the π-conjugated scaffold.

Optoelectronic properties of the heteroatom-doped nanographenes. The steady-state UV-Vis absorption and emission properties of compounds **7**, **11**, **18** and **26** in CH_2Cl_2 are displayed in Figure 9 and summarized in Table 1. The data for reference compounds **HBC** and **2** are also reported for comparison purposes.[33] The absorption envelop for gulf-type molecule **18** appears between 280 and 440 nm, with a very weak lowest-energy α-band centered at 430 nm ($\varepsilon < 1000$ $cm^{-1}M^{-1}$).[70,71]

Table 1. Photophysical data in aerated CH_2Cl_2 and in glassy matrix for molecules **11**, **18**, **26**, **7**, **HBC** and **2**.

Molecule	Absorption		Emission					
	λ [nm] (ε, L mol^{1}cm^{-1}) [a]	$\lambda_{max,fl}$ [nm] [a]	E_{opt} [eV]	τ_{fl} [ns]	Φ_{fl}	$\lambda_{max,ph}$ [nm] [e]	τ_{ph} [s] [e]	$\Delta E_{(H-L)}$ [eV]
11	367 (16250) 362 (11860) 348 (13600) 292 (18500)	371 389 409 430	3.36 [b]	3.37	0.90	–	–	4.23
18	430 (800) 377 (10900) 366 (31300) 332 (70400) 319 (45000) 306 (41500)	408 433 449 458 476	3.11 [c]	<1.0	0.11 [d]	540 584 634	2.7	3.71
26	575 (25027) 539 (9635) 480 (4117) 364 (18116) 343 (23378)	595	2.12 [b]	8.1	0.48	–	–	4.67

7	393 (27730) 373 (17800) 356 (15300) 340 (15700)	403 423 443	3.12	3.5	0.83	486 522 559	1.45	3.73
HBC	446 (1000) 388 (53800) 358 (159100)	485	2.76	16.4	0.03	570	0.8	3.99
2	375 (24000) 314 (31200)	404	3.29	8.2	0.43	492	4.0	3.51

[a] Recorded in an aerated CH_2Cl_2 solution at r.t. [b] Calculated from the lowest energy intersection between absorption and emission spectra normalized on the lowest energy peak (E_{opt} [eV] = $1240.5/\lambda_{cross}$ [nm]). [c] Calculated from the average between the energies of the lowest emission and absorption peak. [d] 9,10-Diphenylanthracene was used as reference standard (0.97 in aerated Cyclohexane).[1] [e] Recorded at 77K in a 1:1 CH_2Cl_2:$CHCl_3$ glassy matrix.

Upon replacement of the central benzene ring with a B_3N_2O congener, a significant blue-shift of the absorption bands is observed, and the lowest-energy structured electronic $\pi\pi^*$ transition appears with a maximum at 367 nm ($\varepsilon \approx 16000$ cm^{-1}M^{-1}). As expected, the spectral envelops of both gulf-type molecules **11** and **18** are blue shifted when compared to those of references **2** and **HBC** (Figure 9). Compound **26** shows a broad unstructured absorption band centered at 575 nm. The substantial redshift of the first electronic transition of **26** compared to that of the other derivatives is probably ascribable to the presence of the oxonium specie that, being electron deficient, could induce a lowering of the HOMO-LUMO transition energy. Remarkably, the absorption spectrum of helicene **7** closely resembles that of molecule **2**. Regarding the emission spectra, boroxadiazine derivative **11** displays the most blue-shifted emission band (λ_{max} = 371 nm, τ_{fl} =3.37 ns, Φ_{fl} = 0.9), followed by **7** (λ_{max} = 403 nm, τ_{fl}= 3.5 ns, Φ_{fl} = 0.83), **18** (λ_{max} = 408 nm, τ_{fl} < 1 ns ns, Φ_{fl} = 0.11) and **26** (λ_{max} = 595 nm, τ_{fl} = 8.1 ns, Φ_{fl} = 0.48). As observed for molecule **2**, derivatives **11**, **7** and **26** display narrow *Stokes* shifts (27 meV, 70 meV and 69 meV, respectively), probably due to the rigid molecular scaffold that prevents most of the geometry-changing vibrational relaxations at the excited state. The all-

carbon gulf-type derivative **18** displays a low emission quantum yield (Φ_{fl} = 0.11), which is, however, three times larger than its parent benzocoronene **HBC** (Φ_{fl} = 0.03). Interestingly, molecules **11** and **26** show strong emissive properties, with Φ_{fl} values equal to 0.9 and 0.5, respectively. In particular, B_3N_2O-doped nanographene **11** shows a two-fold increase of the Φ_{fl} value compared to **2**. Notably, no phosphorescence was detected for molecules **11** and **26** at 77K, while **18** (λ_{max}= 540 nm, τ_{ph} = 2.7s) and helicene **7** (λ_{max}= 486 nm, τ_{ph} = 1.45 s) depict long-lasting phosphorescence emission signals.
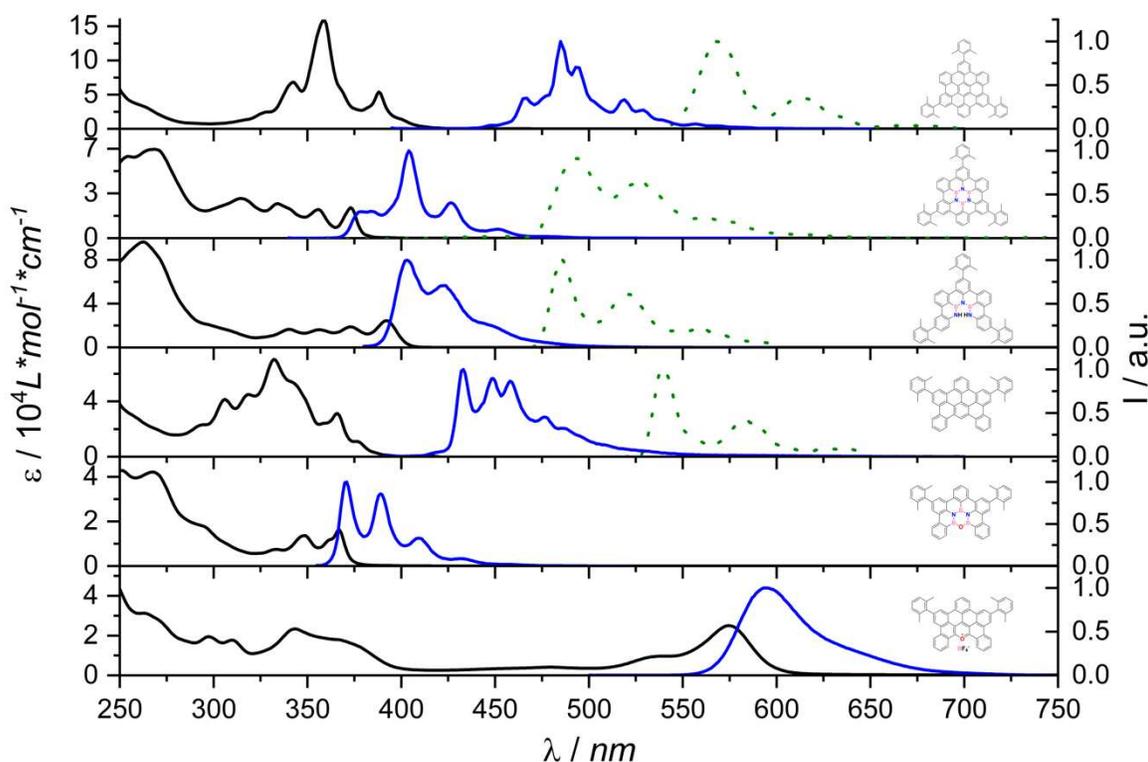

Figure 9. Absorption (—), fluorescence (—) in aerated CH_2Cl_2 solutions at r.t. and phosphorescence (•••) at 77 K in a 1:1 CH_2Cl_2:$CHCl_3$ glassy matrix of **2** (λ_{exc} = 315 nm), **HBC** (λ_{exc} = 355 nm), **11** (λ_{exc} = 265 nm), **7** (λ_{exc} = 350 nm), **18** (λ_{exc} = 265 nm) and **26** (λ_{exc} = 267 nm).

Electrochemical studies were carried out by means of cyclic voltammetry (CV). Surprisingly, only irreversible or quasi-reversible oxidative events were detected, with cathodic peaks ranging between 0.8 and 1.2 V vs Fc^+/Fc (1.09 V, 1.01 V, 0.757 V, and 0.5 V for **11**, **18**, **7**, and **26**, respectively) at the scan rate of 0.2 V s^{-1} (Figure S71). HOMO-LUMO profiles and energy gap were

calculated in vacuum at the B3LYP/6-31+G** level of theory (Figure 10 and S73). As expected, the HOMO-LUMO profiles suggest that the replacement of the central benzene ring with a B_3N_2O cluster causes a widening of the bandgap, resulting in a strong blue-shift of the absorption and emission properties. Surprisingly, helicene **7** shows a similar HOMO-LUMO gap to that of full-carbon gulf-type nanographene **18**. Finally, pyrylium **26** presents the narrowest gap, probably due to the presence of a charge separation state.
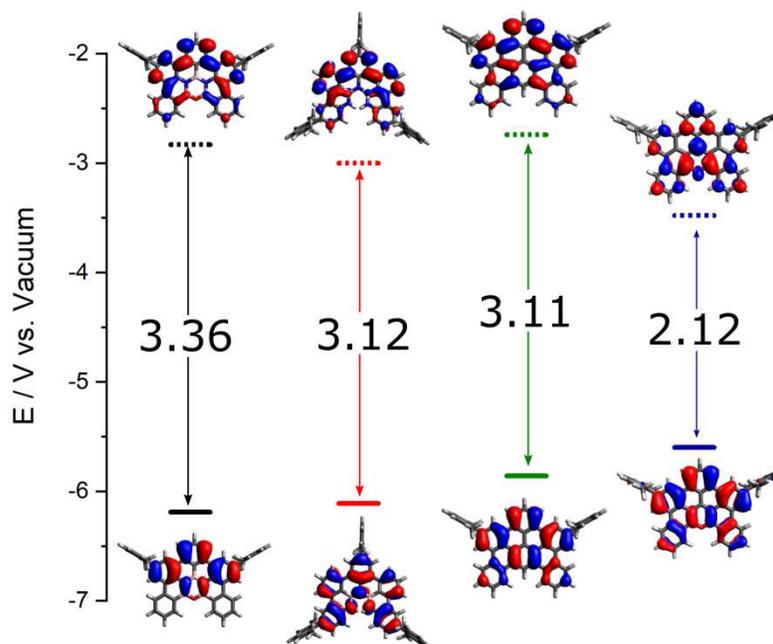

Figure 10. Frontier orbital energies estimated from the CV and photophysical data for **11**, **7**, **18** and **26**. HOMO and LUMO orbitals have been plotted over optimized structures calculated in vacuum at the B3LYP/6-31+G** level of theory using Gaussian09/D01.

Conclusions

In conclusion, it was possible to develop a new strategy towards molecule **2** using a borazine bearing one fluorine atom on the *ortho*-position of each ring. This approach leads to higher yields of **2** and to the unexpected formation of unprecedented B_3N_2O doped PAH **11**. Mechanistic studies on the stepwise cyclisation for both pathways led to a clearer understanding of the reaction

intermediates. A stepwise mechanism proceeding through extension of the π system is highlighted, providing an effective explanation for the presence of byproducts **7, 11, A1** and **A2** in the reaction mixtures. Derivative **11** represents the first example of a B_3N_2O doped PAH and to shed light on the properties arising from this kind of doping NMR, photophysical and computational studies were performed on **11** and its congeners **18** and **26**. These studies underlined for the first time the widening of the HOMO-LUMO gap provided by the substitution of a full-aromatic sextet of the Clar resonance structure with a $B_3N_nO_0$ based ring. NICS(1) studies allowed us to evaluate the effect of doping on aromaticity of this systems, and along with solution NMR, made possible to appreciate the decrease in the magnetic anisotropy arising from borazine based doping of PAHs. Finally, the presence of the gulf region led to an increase in the quantum yield of derivatives **11** and **18** compared to parent compounds **2** and **HBC.** Given the growing importance of doped PAHs and nanographene systems in science, this study represents an important step towards the synthesis of tailored borazino-doped nanographenes. Moreover, the extensive studies performed on all the obtained derivatives provide an important guideline for the design of precisely doped PAHs presenting tailored properties. This result is, therefore, of fundamental importance in the growing field of organic optoelectronic devices.

Additional Information

The authors declare no conflict of interest.

References

[1] A. Narita, X. Wang, X. Feng, K. Müllen, *Chem. Soc. Rev.* **2015**, *44*, 6616–6643.

[2] J. Wang, J. Pei, *Chin. Chem. Lett.* **2016**, *27*, 1139–1146.

[3] D. Bonifazi, F. Fasano, M. M. Lorenzo-Garcia, D. Marinelli, H. Oubaha, J. Tasseroul, *Chem. Commun.* **2015**, *51*, 15222-15236.

[4] M. Stępień, E. Gońka, M. Żyła, N. Sprutta, *Chem. Rev.* **2017**, *117*, 3479-3716.

[5] M. J. D. Bosdet, W. E. Piers, *Can. J. Chem.* **2009**, *87*, 8-29.

[6] X. Y. Wang, J. Y. Wang, J. Pei, *Chem. Eur. J.* **2015**, *21*, 3528-3539.

[7] Z. Liu, T. B. Marder, *Angew. Chem. Int. Ed.* **2008**, *47*, 242-244.

[8] X. Wang, A. Narita, W. Zhang, X. Feng, *J. Am. Chem. Soc.* **2016**, *138*, 9021-9024.

[9] X. Wang, J. I. Urgel, G. B. Barin, K. Eimre, M. Di Giovannantonio, A. Milani, M. Tommasini, C. A. Pignedoli, P. Ru, X. Feng, R. Fasel, K. Müllen, A. Narita, *J. Am. Chem. Soc.* **2018**, *140*, 9104-9107.

[10] X. Wang, T. Dienel, M. Di Giovannantonio, G. B. Barin, N. Kharche, O. Deniz, J. I. Urgel, R. Widmer, S. Stolz, L. H. De Lima, M. Muntwiler, M. Tommasini, V. Meunier, P. Ruffieux, X. Feng, R. Fasel, K. Müllen, A. Narita, *J. Am. Chem. Soc.* **2017**, *139*, 4671-4674.

[11] M. Numano, N. Nagami, S. Nakatsuka, T. Katayama, *Chem. Eur. J.* **2016**, *22*, 11574-11577.

[12] N. Otero, P. Karamanis, K. E. El-Kelany, M. Rérat, L. Maschio, B. Civalleri, B. Kirtman, *J. Phys. Chem. C* **2017**, *121*, 709-722.

[13] P. Karamanis, N. D. Charistos, M. P. Sigalas, M. Re, *J. Phys. Chem. C* **2019**, *123*, 21135-21149.

[14] H. Helten, *Chem. Eur. J.* **2016**, *22*, 12972-12982.

[15] M. M. Lorenzo-García, D. Bonifazi, *Chim. Int. J. Chem.* **2017**, *71*, 550–557.

[16] M. J. D. Bosdet, W. E. Piers, T. S. Sorensen, M. Parvez, *Angew. Chem. Int. Ed.* **2007**, *46*, 4940–4943.

[17] (a) S. Kervyn, N. Kalashnyk, M. Riello, B. Moreton, J. Tasseroul, J. Wouters, T. S. Jones, A. De Vita, G. Costantini, D. Bonifazi, *Angew. Chem. Int. Ed.*, **2013**, *52*, 7410-7412; (b) N. Kalashnyk, P. Ganesh Nagaswaran, S. Kervyn, M. Riello, B. Moreton, T. S. Jones, A. De Vita, D. Bonifazi, G. Costantini, *Chem. Eur. J.* **2014**, *20*, 11856–11862.

[18] W. Auwärter, F. Fasano, N. Demitri, D. Bonifazi, M. Garnica, M. Schwarz, *Chem. Eur. J.* **2018**, *24*, 9565–9571.

[19] C. Sánchez-Sánchez, S. Brüller, H. Sachdev, K. Müllen, M. Krieg, H. F. Bettinger, A. Nicolaï, V. Meunier, L. Talirz, R. Fasel, P. Ruffieux, *ACS Nano* **2015**, *9*, 9228–9235.

[20] C. Zhang, L. Zhang, C. Sun, W. Sun, X. Liu, *Org. Lett.* **2019**, *21*, 3476–3480.

[21] J. S. A. Ishibashi, J. L. Marshall, A. Mazie, G. J. Lovinger, B. Li, L. N. Zakharov, A. Dargelos, A. Graciaa, A. Chrostowska, S. Liu, *J. Am. Chem. Soc.* **2014**, *136*, 15414–15421.

[22] (a) M. Hirai, N. Tanaka, M. Sakai, S. Yamaguchi, *Chem. Rev.* **2019**, *119*, 8291–8331; (b) T. Kaehler, M. Bolte, H. Lerner, M. Wagner, *Angew. Chem. Int. Ed* **2019**, *131*, 11501–11506.

[23] M. Müller, S. Behnle, C. Maichle-Mössmer, H. F. Bettinger, *Chem. Commun.* **2014**, *50*, 7821–7823.

[24] D. L. Crossley, R. J. Kahan, S. Endres, A. J. Warner, R. A. Smith, J. Cid, J. J. Dunsford, J. E. Jones, I. Vitorica-Yrezabal, M. J. Ingleson, *Chem. Sci.* **2017**, *8*, 7969–7977.

[25] D. T. Yang, T. Nakamura, Z. He, X. Wang, A. Wakamiya, T. Peng,

S. Wang, *Org. Lett.* **2018**, *20*, 6741–6745.

[26] (a) X. Wang, F. Zhang, K. S. Schellhammer, P. Machata, F. Ortmann, G. Cuniberti, Y. Fu, J. Hunger, R. Tang, A. A. Popov, R. Berger, K. Müllen, X. Feng, *J. Am. Chem. Soc.* **2016**, 11606–11615; (b) T. Hatakeyama, S. Hashimoto, S. Seki, M. Nakamura, *J. Am. Chem. Soc.* **2011**, *133*, 18614-18617; (c) T. Hatakeyama, K. Shiren, K. Nakajima, S. Nomura, S. Nakatsuka, K. Kinoshita, J. Ni, Y. Ono, T. Ikuta, *Adv. Mater.* **2016**, *28*, 2777-2781; (d) M. Numano, N. Nagami, S. Nakatsuka, T. Katayama, K. Nakajim, S. Tatsumi, N. Yasuda, T. Hatakeyama *Chem. Eur. J.* **2016**, *22*, 11574-11577; (e) K. Matsui, S. Oda, K. Yoshiura, K. Nakajima, N. Yasuda, T. Hatakeyama, *J. Am. Chem. Soc.* **2018**, *140*, 1195-1198

[27] R. Kinney, D. F. Pontz, *J. Am. Chem. Soc.* **1936**, *278*, 197.

[28] R. Oesterle, W. Maringgele, A. Meller, *J. Organomet. Chem.* **1985**, *284*, 281–289.

[29] Y. Kawashima, H. Takeo, C. Matsumura, *Inorg. Chem.* **1989**, *28*, 666–669.

[30] M. Komorowska, K. Niedenzu, W. Weber, *Inorg. Chem.* **1990**, *48*, 289–294.

[31] A. Stock, E. Pohland, *Berichte der Dtsch. Chem. Gesellschaft* **1926**, *59*, 2215–2223.

[32] H. Noda, M. Furutachi, Y. Asada, M. Shibasaki, N. Kumagai, *Nat. Chem.* **2017**, *9*, 571–577.

[33] (a) J. Dosso, J. Tasseroul, F. Fasano, D. Marinelli, N. Biot, A. Fermi, D. Bonifazi, *Angew. Chem. Int. Ed.* **2017**, *56*, 4483–4487; (b) E. Fresta, J. Dosso, J. Cabanillas-González, D. Bonifazi, R. D. Costa, *Adv. Funct. Mater.* **2020**, DOI: 10.1002/adfm.201906830.

[34] M. Krieg, F. Reicherter, P. Haiss, M. Ströbele, K. Eichele,

M. J. Treanor, R. Schaub, H. F. Bettinger, *Angew. Chem. Int. Ed.* **2015**, *54*, 8284–8286.

[35] C. Chen, K. Guo, Y. Zhu, F. Wang, W. Zhang, H. Qi, *Appl. Mater. Interfaces* **2019**, *11*, 33245–33253.

[36] N. Riensch, A. Deniz, S. Kühl, L. Müller, A. Adams, A. Pich, H. Helten, *Polym. Chem.* **2017**, *8*, 5255–5446.

[37] J. Dosso, D. Marinelli, N. Demitri, D. Bonifazi, *ACS Omega* **2019**, *4*, 9343–9351.

[38] S. Behera, K. T. Jackson, H. M. El-Kaderi, T. E. Reich, P. Jena, *J. Mater. Chem.* **2012**, *22*, 13524–13528.

[39] T. E. Reich, K. T. Jackson, S. Li, P. Jena, H. M. El-Kaderi, *J. Mater. Chem.* **2011**, *21*, 10629–10632.

[40] D. Marinelli, F. Fasano, B. Najjari, N. Demitri, D. Bonifazi, *J. Am. Chem. Soc.* **2017**, *139*, 5503–5519.

[41] O. Allemann, S. Duttwyler, P. Romanato, K. K. Baldridge, J. S. Siegel, *Science* **2011**, *332*, 574–577.

[42] O. Anamimoghadam, M. D. Symes, D. Long, S. Sproules, L. Cronin, *J. Am. Chem. Soc.* **2015**, 14944–14951.

[43] O. Anamimoghadam, M. D. Symes, C. Busche, D. Long, S. T. Caldwell, C. Flors, S. Nonell, L. Cronin, *Org. Lett.* **2013**, *15*, 2970–2973.

[44] F. Pina, M. J. Melo, C. A. T. Laia, A. J. Parola, J. C. Lima, *Chem. Soc. Rev.* **2012**, 869–908.

[45] D. Wu, W. Pisula, M. C. Haberecht, X. Feng, K. Müllen, *Org. Lett.* **2009**, *11*, 5686–5689.

[46] C. L. Hilton, J. M. Crowfoot, P. Rempala, B. T. King, *J. Am. Chem. Soc.* **2008**, *130*, 13392–13399.

[47] D. K. Straub, *J. Chem. Educ.* **1995**, *72*, 494–497.

[48] J. M. Robertson, J. Trotter, *J. Chem. Soc.* **1961**, 1280-1284.

[49] R. Goddard, M. W. Haenel, W. C. Herndon, C. Kriiger, M. Zander, *J. Am. Chem. Soc.* **1995**, *117*, 30-41.

[50] A. Le Bail, H. Duroy, J. L. Fourquet, *Mat. Res. Bull.* **1988**, *23*, 447-452.

[51] A. C. Larson, R. B. Von Dreele, *Los Alamos National Laboratory Report,* **2004**, *LAUR*, 86-748.

[52] K. D. M. Harris, *Top Curr. Chem.* **2012**, *315*, 133-178.

[53] K. D. M. Harris, M. Tremayne, P. Lightfoot, P. G. Bruce, *J. Am. Chem. Soc.* **1994**, *116*, 3543-3547.

[54] K. D. M. Harris, S. Habershon, E. Y. Cheung, R. L. Johnston, *Z. Krist.* **2004**, *219*, 838-846.

[55] B. M. Kariuki, P. Calcagno, D. M. Kenneth, D. Philp, R. L. Johnston, *Angew. Chem. Int. Ed* **1999**, *38*, 831-835.

[56] B. M. Kariuki, K. Psallidas, K. D. M. Harris, R. L. Johnston, R. W. Lancaster, S. E. Staniforth, S. M. Cooper, *Chem. Commun.* **1999**, 1677-1678.

[57] D. Albesa-jove, B. M. Kariuki, S. J. Kitchin, L. Grice, E. Y. Cheung, K. D. M. Harris, *ChemPhysChem* **2004**, *5*, 414-418.

[58] F. Guo, J. Martı, Z. Pan, C. E. Hughes, K. D. M. Harris, *J. Phys. Chem. C* **2008**, *112*, 19793-19796.

[59] P. A. Williams, C. E. Hughes, G. K. Lim, B. M. Kariuki, K. D. M. Harris, *Cryst. Growth Des.* **2012**, *12*, 3104-3113.

[60] C. E. Hughes, G. M. Manjunatha Reddy, S. Masiero, S. P. Brown, A. P. Williams, K. D. M. Harris, *Chem. Sci.* **2017**, *8*, 3971-3979.

[61] O. Al Rahal, C. E. Hughes, P. A. Williams, A. J. Logsdail, Y. Diskin-posner, K. D. M. Harris, *Angew. Chem. Int. Ed* **2019**,

131, 18964–18968.

[62] R. Desiraju, Gautam, A. Gavezzotti, *J. Am. Chem. Soc.* **1989**, *26*, 621–623.

[63] G. S. Hammond, *J. Am. Chem. Soc.* **1955**, 77, 334–338.

[64] T. Yanai, D. P. Tew, N. C. Handy, *Chem. Phys. Lett.* **2004**, *393*, 51–57.

[65] W. J. Hehre, R. Ditchfield, J. A. Pople, **1972**, *52*, 2257–2561.

[66] W. C. M. J. Frisch, G. W. Trucks, H. B. Schlegel, G. E. Scuseria, M. A. Robb, J. R. Cheeseman, G. Scalmani, V. Barone, B. Mennucci, G. A. Petersson, H. Nakatsuji, M. Caricato, X. Li, H. P. Hratchian, A. F. Izmaylov, J. Bloino, G. Zheng, J. L. Sonnenberg, M. Had, *Gaussian 09, Revis. D.01, Gaussian Inc., Wallingford CT* **2010**.

[67] J. Tomasi, B. Mennucci, R. Cammi, *Chem. Rev.* **2005**, *105*, 2999–3093.

[68] A. Suzuki, *Pure Appl. Chem.* **1994**, *66*, 213–222.

[69] M. Randic, *Chem. Rev.* **2003**, 3449–3605.

[70] M. Daigle, A. Picard-Lafond, E. Soligo, J. F. Morin, *Angew. Chem. Int. Ed.* **2016**, *55*, 2042–2047.

[71] C. Kübel, K. Eckhardt, V. Enkelmann, G. Wegner, K. Müllen, *J. Mater. Chem.* **2000**, *10*, 879–886.